Title

Three-dimensional focusing through scattering media using conjugate adaptive optics with remote focusing (CAORF).

Journal

Optics express, 25(9)

ISSN

1094-4087

Authors

Tao, Xiaodong
Lam, Tuwin
Zhu, Bingzhao
et al.

Publication Date

2017-05-01

Peer reviewed

Research Article | Vol. 25, No. 9 | 1 May 2017 | OPTICS EXPRESS 10368

Optics EXPRESS

Three-dimensional focusing through scattering media using conjugate adaptive optics with remote focusing (CAORF)

XIAODONG TAO,[1,*] TUWIN LAM,[1] BINGZHAO ZHU,[2] QINGGELE LI,[1] MARC R. REINIG,[1] AND JOEL KUBBY[1]

[1]*W.M. Keck Center for Adaptive Optical Microscopy, Jack Baskin School of Engineering, University of California, Santa Cruz, CA 95064, USA*

[2]*State Key Laboratory of Modern Optical Instrumentation, College of Optical Science and Engineering and the Collaborative Innovation Center for Brain Science, Zhejiang University, Hangzhou, Zhejiang 310027, China*

[*]*xiaod.tao@gmail.com*

Abstract: The small correction volume for conventional wavefront shaping methods limits their application in biological imaging through scattering media. We demonstrate large volume wavefront shaping through a scattering layer with a single correction by conjugate adaptive optics and remote focusing (CAORF). The remote focusing module can maintain the conjugation between the adaptive optical (AO) element and the scattering layer during three-dimensional scanning. This new configuration provides a wider correction volume by better utilization of the memory effect in a fast three-dimensional laser scanning microscope. Our results show that the proposed system can provide 10 times wider axial field of view compared with a conventional conjugate AO system when 16,384 segments are used on a spatial light modulator. We also demonstrate three-dimensional fluorescence imaging, multi-spot patterning through a scattering layer and two-photon imaging through mouse skull tissue.

OCIS codes: (110.0113) Imaging through turbid media; (290.4210) Multiple scattering; (110.0180) Microscopy; (110.7050) Turbid media; (110.1080) Active or adaptive optics.

References and links

1. W. Denk, J. H. Strickler, and W. W. Webb, "Two-photon laser scanning fluorescence microscopy," Science **248**(4951), 73–76 (1990).
2. F. Helmchen and W. Denk, "Deep tissue two-photon microscopy," Nat. Methods **2**(12), 932–940 (2005).
3. N. G. Horton, K. Wang, D. Kobat, C. G. Clark, F. W. Wise, C. B. Schaffer, and C. Xu, "In vivo three-photon microscopy of subcortical structures within an intact mouse brain," Nat. Photonics **7**(3), 205–209 (2013).
4. D. Kobat, N. G. Horton, and C. Xu, "In vivo two-photon microscopy to 1.6-mm depth in mouse cortex," J. Biomed. Opt. **16**(10), 106014 (2011).
5. X. Tao, H. Lin, T. Lam, R. Rodriguez, J. W. Wang, and J. Kubby, "Transcutical imaging with cellular and subcellular resolution," Biomed. Opt. Express **8**(3), 1277–1289 (2017).
6. D. Débarre, E. J. Botcherby, T. Watanabe, S. Srinivas, M. J. Booth, and T. Wilson, "Image-based adaptive optics for two-photon microscopy," Opt. Lett. **34**(16), 2495–2497 (2009).
7. P. Marsh, D. Burns, and J. Girkin, "Practical implementation of adaptive optics in multiphoton microscopy," Opt. Express **11**(10), 1123–1130 (2003).
8. N. Ji, D. E. Milkie, and E. Betzig, "Adaptive optics via pupil segmentation for high-resolution imaging in biological tissues," Nat. Methods **7**(2), 141–147 (2010).
9. X. Tao, B. Fernandez, O. Azucena, M. Fu, D. Garcia, Y. Zuo, D. C. Chen, and J. Kubby, "Adaptive optics confocal microscopy using direct wavefront sensing," Opt. Lett. **36**(7), 1062–1064 (2011).
10. X. Tao, J. Crest, S. Kotadia, O. Azucena, D. C. Chen, W. Sullivan, and J. Kubby, "Live imaging using adaptive optics with fluorescent protein guide-stars," Opt. Express **20**(14), 15969–15982 (2012).
11. M. J. Booth, "Adaptive optics in microscopy," Philos Trans A Math Phys Eng Sci **365**(1861), 2829–2843 (2007).
12. J. A. Kubby, ed., *Adaptive Optics for Biological Imaging* (CRC, Taylor & Francis Group, 2013).
13. A. P. Mosk, A. Lagendijk, G. Lerosey, and M. Fink, "Controlling waves in space and time for imaging and focusing in complex media," Nat. Photonics **6**(5), 283–292 (2012).
14. Z. Yaqoob, D. Psaltis, M. S. Feld, and C. Yang, "Optical phase conjugation for turbidity suppression in biological samples," Nat. Photonics **2**(2), 110–115 (2008).

#286627 https://doi.org/10.1364/OE.25.010368
Journal © 2017 Received 17 Feb 2017; revised 18 Apr 2017; accepted 18 Apr 2017; published 26 Apr 2017

Optics EXPRESS

15. M. Cui and C. Yang, "Implementation of a digital optical phase conjugation system and its application to study the robustness of turbidity suppression by phase conjugation," Opt. Express **18**(4), 3444–3455 (2010).
16. E. H. Zhou, H. Ruan, C. Yang, and B. Judkewitz, "Focusing on moving targets through scattering samples," Optica **1**(4), 227–232 (2014).
17. I. M. Vellekoop and A. P. Mosk, "Focusing coherent light through opaque strongly scattering media," Opt. Lett. **32**(16), 2309–2311 (2007).
18. I. M. Vellekoop, "Feedback-based wavefront shaping," Opt. Express **23**(9), 12189–12206 (2015).
19. D. B. Conkey, A. N. Brown, A. M. Caravaca-Aguirre, and R. Piestun, "Genetic algorithm optimization for focusing through turbid media in noisy environments," Opt. Express **20**(5), 4840–4849 (2012).
20. O. Katz, E. Small, Y. Guan, and Y. Silberberg, "Noninvasive nonlinear focusing and imaging through strongly scattering turbid layers," Optica **1**(3), 170–174 (2014).
21. S. M. Popoff, G. Lerosey, R. Carminati, M. Fink, A. C. Boccara, and S. Gigan, "Measuring the transmission matrix in optics: an approach to the study and control of light propagation in disordered media," Phys. Rev. Lett. **104**(10), 100601 (2010).
22. S. M. Popoff, A. Goetschy, S. F. Liew, A. D. Stone, and H. Cao, "Coherent control of total transmission of light through disordered media," Phys. Rev. Lett. **112**(13), 133903 (2014).
23. S. Feng, C. Kane, P. A. Lee, and A. D. Stone, "Correlations and fluctuations of coherent wave transmission through disordered media," Phys. Rev. Lett. **61**(7), 834–837 (1988).
24. I. Freund, M. Rosenbluh, and S. Feng, "Memory effects in propagation of optical waves through disordered media," Phys. Rev. Lett. **61**(20), 2328–2331 (1988).
25. I. M. Vellekoop and C. M. Aegerter, "Scattered light fluorescence microscopy: imaging through turbid layers," Opt. Lett. **35**(8), 1245–1247 (2010).
26. C. L. Hsieh, Y. Pu, R. Grange, G. Laporte, and D. Psaltis, "Imaging through turbid layers by scanning the phase conjugated second harmonic radiation from a nanoparticle," Opt. Express **18**(20), 20723–20731 (2010).
27. X. Yang, C. L. Hsieh, Y. Pu, and D. Psaltis, "Three-dimensional scanning microscopy through thin turbid media," Opt. Express **20**(3), 2500–2506 (2012).
28. O. Katz, E. Small, and Y. Silberberg, "Looking around corners and through thin turbid layers in real time with scattered incoherent light," Nat. Photonics **6**(8), 549–553 (2012).
29. J. Ryu, M. Jang, T. J. Eom, C. Yang, and E. Chung, "Optical phase conjugation assisted scattering lens: variable focusing and 3D patterning," Sci. Rep. **6**, 23494 (2016).
30. G. Ghielmetti and C. M. Aegerter, "Scattered light fluorescence microscopy in three dimensions," Opt. Express **20**(4), 3744–3752 (2012).
31. J. H. Park, W. Sun, and M. Cui, "High-resolution in vivo imaging of mouse brain through the intact skull," Proc. Natl. Acad. Sci. U.S.A. **112**(30), 9236–9241 (2015).
32. S. Schott, J. Bertolotti, J. F. Léger, L. Bourdieu, and S. Gigan, "Characterization of the angular memory effect of scattered light in biological tissues," Opt. Express **23**(10), 13505–13516 (2015).
33. J. Tang, R. N. Germain, and M. Cui, "Superpenetration optical microscopy by iterative multiphoton adaptive compensation technique," Proc. Natl. Acad. Sci. U.S.A. **109**(22), 8434–8439 (2012).
34. D. B. Conkey, A. M. Caravaca-Aguirre, and R. Piestun, "High-speed scattering medium characterization with application to focusing light through turbid media," Opt. Express **20**(2), 1733–1740 (2012).
35. X. Tao, D. Bodington, M. Reinig, and J. Kubby, "High-speed scanning interferometric focusing by fast measurement of binary transmission matrix for channel demixing," Opt. Express **23**(11), 14168–14187 (2015).
36. X. Zhang and P. Kner, "Binary wavefront optimization using a genetic algorithm," J. Opt. **16**(12), 125704 (2014).
37. D. Sinefeld, H. P. Paudel, D. G. Ouzounov, T. G. Bifano, and C. Xu, "Adaptive optics in multiphoton microscopy: comparison of two, three and four photon fluorescence," Opt. Express **23**(24), 31472–31483 (2015).
38. P. T. Galwaduge, S. H. Kim, L. E. Grosberg, and E. M. C. Hillman, "Simple wavefront correction framework for two-photon microscopy of in-vivo brain," Biomed. Opt. Express **6**(8), 2997–3013 (2015).
39. G. Duemani Reddy, K. Kelleher, R. Fink, and P. Saggau, "Three-dimensional random access multiphoton microscopy for functional imaging of neuronal activity," Nat. Neurosci. **11**(6), 713–720 (2008).
40. P. A. Kirkby, K. M. Srinivas Nadella, and R. A. Silver, "A compact Acousto-Optic Lens for 2D and 3D femtosecond based 2-photon microscopy," Opt. Express **18**(13), 13720–13745 (2010).
41. B. F. Grewe, F. F. Voigt, M. van 't Hoff, and F. Helmchen, "Fast two-layer two-photon imaging of neuronal cell populations using an electrically tunable lens," Biomed. Opt. Express **2**(7), 2035–2046 (2011).
42. J. M. Jabbour, B. H. Malik, C. Olsovsky, R. Cuenca, S. Cheng, J. A. Jo, Y.-S. L. Cheng, J. M. Wright, and K. C. Maitland, "Optical axial scanning in confocal microscopy using an electrically tunable lens," Biomed. Opt. Express **5**(2), 645–652 (2014).
43. L. Kong, J. Tang, J. P. Little, Y. Yu, T. Lämmermann, C. P. Lin, R. N. Germain, and M. Cui, "Continuous volumetric imaging via an optical phase-locked ultrasound lens," Nat. Methods **12**(8), 759–762 (2015).
44. E. J. Botcherby, R. Juskaitis, M. J. Booth, and T. Wilson, "Aberration-free optical refocusing in high numerical aperture microscopy," Opt. Lett. **32**(14), 2007–2009 (2007).
45. G. Katona, G. Szalay, P. Maák, A. Kaszás, M. Veress, D. Hillier, B. Chiovini, E. S. Vizi, B. Roska, and B. Rózsa, "Fast two-photon in vivo imaging with three-dimensional random-access scanning in large tissue volumes," Nat. Methods **9**(2), 201–208 (2012).

Optics EXPRESS

46. W. Yang, J. E. Miller, L. Carrillo-Reid, E. Pnevmatikakis, L. Paninski, R. Yuste, and D. S. Peterka, "Simultaneous Multi-plane Imaging of Neural Circuits," Neuron **89**(2), 269–284 (2016).
47. H. P. Paudel, J. Taranto, J. Mertz, and T. Bifano, "Axial range of conjugate adaptive optics in two-photon microscopy," Opt. Express **23**(16), 20849–20857 (2015).
48. J. Li, D. R. Beaulieu, H. Paudel, R. Barankov, T. G. Bifano, and J. Mertz, "Conjugate adaptive optics in widefield microscopy with an extended-source wavefront sensor," Optica **2**(8), 682–688 (2015).
49. J. Mertz, H. Paudel, and T. G. Bifano, "Field of view advantage of conjugate adaptive optics in microscopy applications," Appl. Opt. **54**(11), 3498–3506 (2015).
50. T. W. Wu and M. Cui, "Numerical study of multi-conjugate large area wavefront correction for deep tissue microscopy," Opt. Express **23**(6), 7463–7470 (2015).
51. I. M. Vellekoop, "Controlling the propagation of light in disordered scattering media," PhD Thesis (University of Twente, 2008).

1. Introduction

High-resolution optical imaging through scattering media is extremely important for noninvasive biological imaging. Most optical imaging systems rely on ballistic light transmitted through a biological sample to form an image. As the imaging depth increases, multiple scattering becomes a dominant factor limiting the image depth. One way to minimize the scattering effect is to use long wavelength light since the longer wavelength gives less scattering [1,2]. The use of longer wavelength excitation in multiphoton imaging systems has been successfully demonstrated for in-vivo imaging of live animals with extended penetration depth [1–5]. However, special laser systems with low-repetition rate, higher-pulse energy and additional dispersion compensation are required to achieve an acceptable signal-to-noise-ratio with minimal photodamage or photobleaching. In addition, the increase of water absorption can limit the imaging depth when some common laser wavelengths such as 1550 nm are used [3]. Another promising way is to shape the wavefront using adaptive optics (AO). AO has been used to correct low-order aberrations from refractive index mismatch in biological samples [6–12]. High-order wavefront shaping methods for compensation of scattering have been investigated extensively in recent years [13]. The complex wavefront from scattering media can be recorded directly using interferometric techniques and then the desired optical field can be replayed by optical or digital phase conjugation [14–16]. The desired compensation wavefront can also be estimated by feed-back optimization algorithms or transmission matrix measurements [17–22]. The first demonstration of focusing through scattering media by Vellekoop et al. [17] showed its potential for applications in fluorescent laser scanning microscopy. Several groups [23–29] further demonstrated the lateral or axial scanning of the focus behind the scattering layer utilizing the memory effect. Lateral scanning is realized by either rotating the beam around the scanning layers or by adding tip/tilt to the compensation phase. Three-dimensional scanning through a scattering medium has also been demonstrated using a high-speed scanning mirror and a spatial light modulator (SLM) [30]. Additional quadratic phase is applied on the SLM to provide axial scanning. However, the conventional laser scanning system is often translated at the object plane using a high-speed scanner. Furthermore, the slow lateral or axial scanning obtained by updating the phase on a spatial light modulator (SLM) cannot meet the temporal requirement for in vivo biological imaging. Recently, a conjugate AO (CAO) multiphoton system has been demonstrated for high-resolution in-vivo imaging of neurons through a mouse skull [31]. Scattering from the mouse skull is compensated by a segmented deformable mirror that is conjugated with the skull. Since the conjugation plane moves during axial scanning, the results show a limited axial field of view (FOV) that is only tens of microns.

In this paper, we take advantage of CAO and remote focusing (CAORF) to achieve three-dimensional (3D) scanning through a scattering layer with a single correction. The axial scanning is achieved without changing the conjugation by a remote focusing (RF) module. By using a high-speed RF module, this method has the potential to extend its applications to high-speed volumetric imaging through scattering layers, such as transcranial or transcuticular functional imaging. This paper also gives thorough simulations and

Optics EXPRESS

experimental analysis of both CAORF and the conventional CAO without RF, which shows the benefits of maintaining conjugation during axial scanning. In additional, the proposed system rotates the beam at the objective pupil plane instead of at the conjugate plane at the scattering layers [29,31]. It can be easily integrated into a conventional laser scanning fluorescent microscope. This design is also capable of compensating both highly and weakly scattering (refractive aberration) tissues. It does not depend on the highly scattering layer to focus light on the target.

2. Concept

Three configurations of the AO laser scanning systems are shown in Figs. 1(a-c). The conventional pupil AO configuration projects the phase on the SLM to the pupil plane of the objective, as shown in Fig. 1(a). The conjugate plane shifts laterally and axially during 3d scanning. This setup is efficient for compensating low-order refractive aberration, where the FOV is limited by the transverse correlation length σ_x of the distorted wavefront. For highly scattering media, where the transverse correlation length of the distorted wavefront is much smaller than the SLM segment size, this configuration gives a very limited lateral and axial FOV. The lateral FOV is determined by [28]:

$$X_{FOV} \sim 2\sigma_{SLM}, \tag{1}$$

where σ_{SLM} is the SLM segment size on the conjugate plane. When the scattering layer or the objective shifts along the Z-axis, Δ_Z, the segment phase on the scattering layer is rescaled along the optical axis because of the beam convergence, as shown in Fig. 1(a). The effective area in each channel for scattering compensation decreases with the axial shift. The ratio of the intensity at the Δ_Z plane to that at the initial conjugate plane becomes:

$$\eta_{\Delta z} \sim \left(\frac{\sum_n \alpha_{n,\Delta z}}{N} \right)^2, \tag{2}$$

where $\alpha_{n,\Delta Z}$ is the ratio of the effective area to the segment area at the n^{th} segment (see Appendix, A). At the conjugate plane, $\alpha_{n,\Delta Z} = 1$. N is the total number of segments.

The CAO projects the SLM onto the scattering layer as shown in Fig. 1(b). It provides a wider lateral FOV, determined by the optical 'memory effect' for the speckle correlations [23,24]. The lateral FOV is defined by the full width at $1/e^2$ of the intensity correlation (Eq. (12), which is $X_{FOV,e2} \sim 2.686Z\lambda/\pi L$ [32]. L is the thickness of the scattering layer. Z is the distance between the scattering layer and the focal plane. However, this configuration does not maintain conjugation during axial scanning when translating the sample. The axial FOV is the same as the pupil AO system, determined by Eq. (2).

To extend the axial FOV, a new method, integrating an RF module into a CAO system, also called CAORF, is proposed as shown in Fig. 1(c). The purpose of the RF module is to shift the focal plane without moving the sample or the objective lens. This maintains the conjugation between the wavefront corrector and the scattering layer during 3d scanning. Now the axial FOV becomes [28]:

$$Z_{FOV} \sim 2ZX_{FOV} / D, \tag{3}$$

where D is the diameter of the beam on the scattering layer. As can be seen, the axial FOV is not related to the SLM segment number or size. The CAORF can provide a wide-axial FOV even when a large number of segments are used. Equation (3) does not consider the change of the effective area during 3D scanning. Analysis that is more rigorous is made by numerically calculating the memory-effect intensity correlations with both lateral and axial shifts [see Appendix, B].

Optics EXPRESS

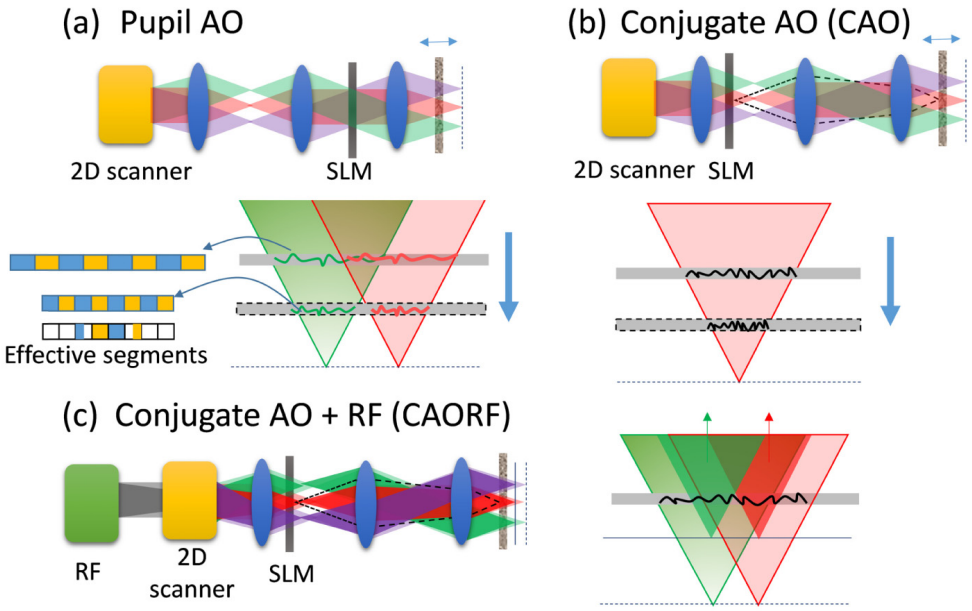

Fig. 1. A schematic diagram of AO laser scanning systems. (a) Pupil AO. The SLM is conjugated with the pupil plane. The projected wavefront at the scattering layer moves with the scanning beam. The effective number of segments decreases with the axial shift. (b) Conjugate AO (CAO). The SLM is located at the plane that is conjugate to the scattering layer. The projected phase changes with the axial shift. (c) CAO and remote focusing (CAORF). The projected phase on the scattering layer does not change during three-dimensional scanning.

3. Experimental setup

Figure 2 shows the system setup to evaluate this new configuration. A solid-state laser (488 nm, LuxX 488-60, Omicron) is used as the light source for both FOV evaluation and fluorescent imaging. It is collimated by an achromatic lens L1 (f = 150mm). As a proof-of-concept system, an achromatic lens L2 (f = 100mm) installed on a three-axis motorized stage works as the RF and two-dimensional (2d) scanning module. Lateral scanning on the sample is realized by the translation of the lens along the X-Y axis. Translation along the *Z*-axis shifts the focal plane without moving the objective lens or the sample. For real biological imaging applications, a fast 2d scanner and a RF module can be used instead. The conjugate AO module includes a reflective SLM (RCL-2500, Holoeye) and a folding mirror M1 installed on a translation stage. Lens L3 (f = 100mm) and an objective lens O1 (10x, NA0.3, LEITZ) projects the phase on the SLM onto the scattering layer. The conjugation planes are aligned precisely by the translation stage without changing the final focal plane. Light from the sample is collected by another objective lens O2 (20x, NA 0.5, LEITZ) and then focused on a CCD camera (Genie M1400-1/2, Teledyne DALSA) by a lens L4 (f = 150mm). For fluorescent imaging, an emission filter (FF01-542/27, Semrock) is put in the detection path, which is not shown in Fig. 2. Single sided tape (Scotch, 3M) attached on a coverslip is used as the scattering layer [16]. The sample is mounted on a translation stage for precise adjustment.

Optics EXPRESS

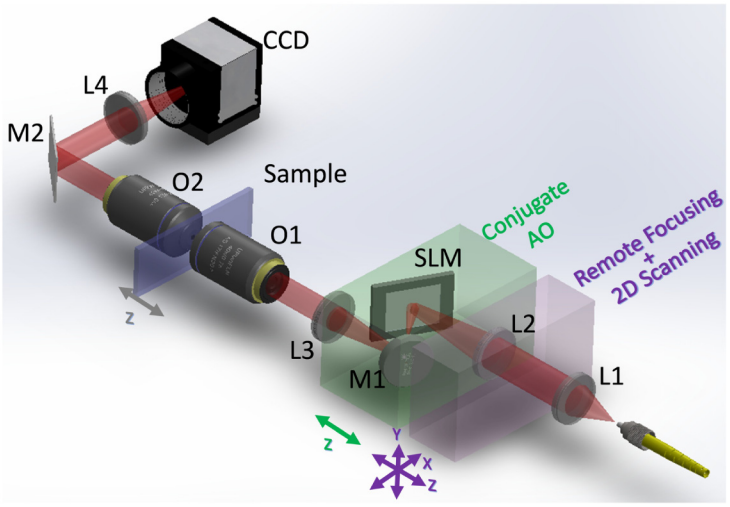

Fig. 2. Schematic of the experimental setup. A lens (L1) collimates the laser beam from a 488nm solid-state laser. A lens (L2) installed on a three-axis translation stage works as a remote focusing (RF) and two-dimensional (2D) scanning module. The conjugate AO module consists of a spatial light modulator (SLM) and a folding mirror (M1), which are installed on a single-axis translation stage. The lens (L3) and an objective lens (O1) image the SLM plane onto the scattering lay. The light is collected by another objective lens (O2) and focused by a lens (L4) on a CCD camera.

4. Wavefront shaping by measuring transmission matrix

An enhanced focus is generated at the backside of the scattering layer by measuring the transmission matrix (TM), T, at the target position [21]. To utilize the full aperture and increase the signal-to-noise-ratio during the TM measurement, the whole aperture is divided into two groups by random selection of half of the segments, as shown in Fig. 3(a). Two measurement steps for those two groups are carried out. In the first step, the first group is selected as the active group and each mode defined by the Hadamard basis is displayed on the SLM. The element of the observed TM for each mode, t_{obs}^{i}, is calculated from the intensities $\left(I_i^0, I_i^{\pi/2}, I_i^{\pi}, I_i^{3\pi/2}\right)$, when the phase of the reference group changes from 0 to 2π using a four-phase method [21]:

$$t_{obs}^{i} = (I_i^0 - I_i^{\pi})/4 + (I_i^{3\pi/2} - I_i^{\pi/2})/4. \quad (4)$$

After the first measurement, the final input phase E_{in} is calculated:

$$E_{in} = T_{obs}^{'} \Big/ \left|T_{obs}^{'}\right|, \quad (5)$$

and is updated on the first group as shown in Fig. 3(b). Then the same procedure is performed on the other group to achieve the final phase mask, as shown in Fig. 3(c). Figures 3(d-f) show the focus before correction, and after the first and second steps, respectively. The intensity is doubled after the second correction, as expected. Compared with direct phase measurement using optical phase conjugation [14,15], it is more practical for fluorescent imaging, where the emission light is incoherent. The measurement time is limited by the frame rate of the SLM. Currently, the total measurement time for 1024 channels is 135 seconds. Since only a single correction is required for 3d scanning, it is tolerable when imaging through a static scattering layer. Potentially the measurement time could be reduced to less than half a second when a high-speed segmented deformable mirror or a digital micro mirror device is used [33–36]. To analyze the system performance, we measured the transmission matrix using light

Optics EXPRESS

from the back surface of the sample, which gives a high signal-to-noise ratio. In the two-photon imaging though mouse skull tissue, the epifluorescence was used for phase shaping.

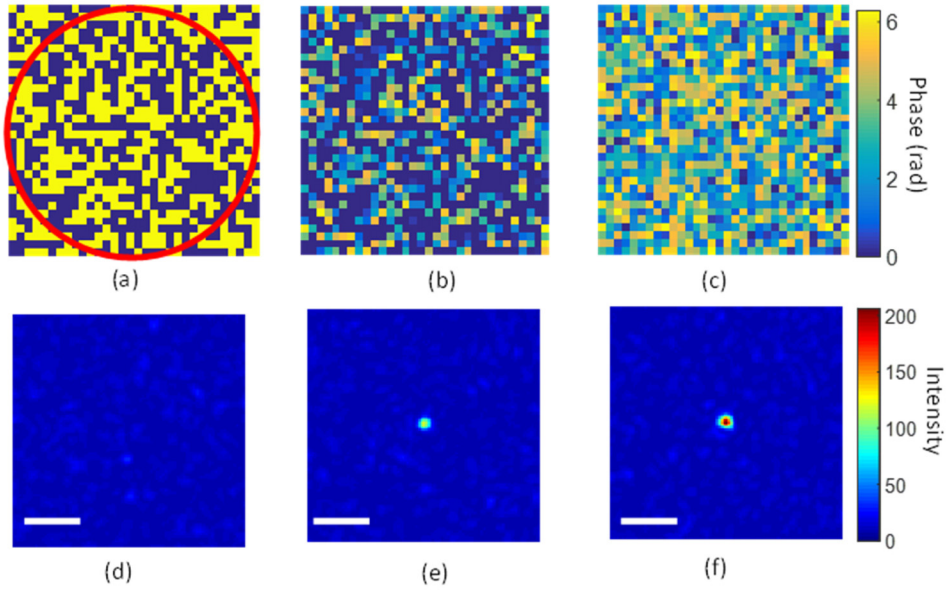

Fig. 3. Wavefront shaping by measuring the transmission matrix. (a) The whole aperture is randomly divided into two groups of segments. (b) The optimal phase of the first group after the transmission matrix measurement. (c) After the optimal phase for the second group of segments is achieved, the combined phase mask is displayed on the SLM. The image before correction, after the first correction and after the second correction are shown in (d), (e) and (f) respectively. The scale bar is 5 μm.

5. Experimental results

5.1 3D Focusing through scattering layers

To evaluate the ability for 3d focusing through the scattering layer, a coverslip with a strip of scattering tape is placed 2 mm from the focal plane of lens O1. Then lens O2 is moved accordingly to focus on the scattering layer. The conjugate AO module is adjusted to the conjugate plane of the scattering layer. The correct conjugation is verified by imaging both the SLM and the scattering layer on the camera. Then lens O2 moves back to the focal plane of lens O1 for monitoring the focal spot. The transmission matrix measurement is performed to generate an interferometric focus behind the scattering layer. To evaluate the focal spot in 3d space, the beam is scanned in the X-Z plane by the RF and 2d scanning modules, as shown in Fig. 4 (a). The objective lens O2 is refocused at each new depth to monitor the focus at different depths. To compare with the results without RF, the scattering layer is moved along the Z-axis as shown in Fig. 4(b). The normalized peak intensity of the focal spot along the X-Z plane with RF and without RF is shown in Fig. 4(c) and Fig. 4(d), respectively. The CAORF gives a much slower intensity drop with an axial shift in comparison to one without RF. The simulation of the CAORF shows a similar intensity drop with the axial shift [see Fig. 12(b) in Appendix B]. Figure 4(e) shows the normalized peak intensity of the spot at the center of the field at different axial shifts. The red and blue dashed lines indicate the measurement data for the configurations with and without RF, respectively. The axial FOV measured by the full-width-half-maximum (FWHM) increases from 0.1 mm to 0.43 mm when RF is applied. The simulation result is indicated by the blue line. The deviation from the experimental result could be caused by misalignment and conjugation errors from the tilted SLM.

Optics EXPRESS

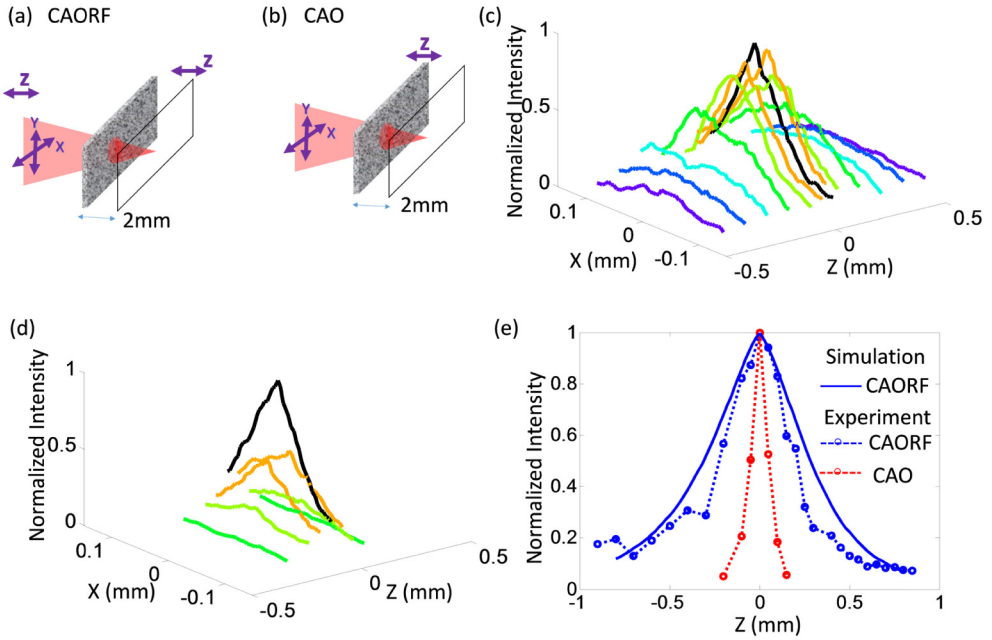

Fig. 4. Field of view analysis for 3d scanning for CAORF (a) and CAO without RF (b). The normalized intensity of the focal spot scanning along the X-Z plane for these two configurations are shown in (c) and (d), respectively. (e) The normalized intensity of the focal spot along the center of the field versus the axial shift. The red and blue dashed curves show measurement results for CAORF and CAO, respectively. The simulation of CAORF (a) is indicated by the blue curve.

Another advantage of CAORF is the insensitivity of the axial FOV to the number of segments on the SLM. A full TM is often comprised of millions of elements. Even a small fraction of the full matrix still requires thousands of channels on the SLM. For a large number of segments, the focus will be lost even with a small conjugation error caused by the focus shift. Using RF to maintain the conjugation between the SLM and the scattering layer, the axial FOV is only determined by the memory effect. Figure 5 shows the normalized intensity of the focus at various focal distances with 1024, 4096 and 16,384 segments on the SLM. The measurements with CAORF are indicated by the triangles. The results with different numbers of segments have a similar intensity drop with the axial shift, which is around 200 μm at the half-width-half-maximum (HWHM). However, without RF, the configuration with more segments gives a much smaller axial FOV. The HWHMs for 1024, 4096 and 16,384 segments drop to 40 μm, 27 μm and 19 μm, respectively. Figure 5 also shows the simulations in different situations based on Eq. (2) and Eq. (12) (see Appendix, A and B). The difference between the measurement and simulations could be caused by the alignment error or the conjugation error from a tilted SLM. The results show the improvement of the axial FOV by 5, 7 and 10 times for 1024, 4096 and 16,384 segments, respectively.

Optics EXPRESS

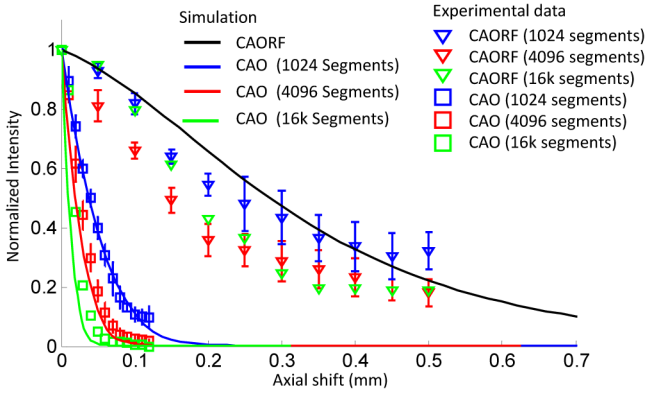

Fig. 5. Effect of the axial shift on the normalized intensity of the focal spot for different numbers of segments with CAORF and CAO. The measurements with CAORF and CAO are indicated by triangles and squares. The solid curves shows the simulation results in each case. The results for 1024, 4096 and 16,384 segments are indicated by blue, red and green, respectively.

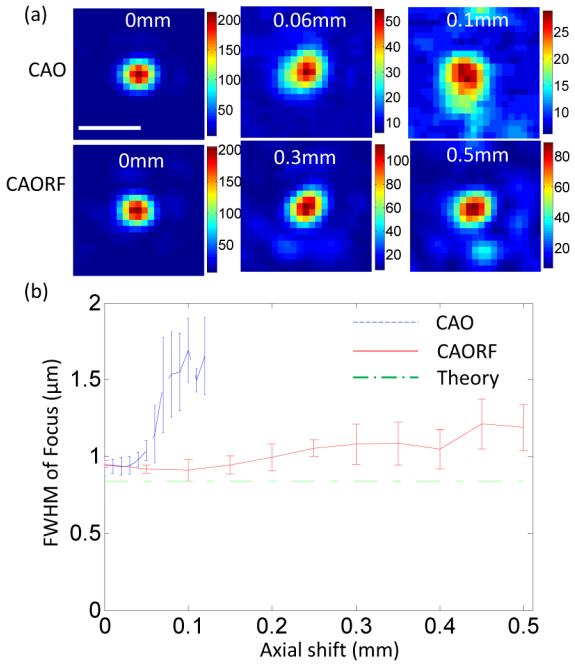

Fig. 6. (a) Images of the focal spot at different focal planes for CAO and CAORF. (b) The full-width-half-maximum (FWHM) of the focal spot at different focal distances. The measurements for CAO and CAORF are indicated by blue and red lines. The theoretical resolution is indicated by the green line. The scale bar is 2μm.

The theoretical FWHM of the focal spot for a circular aperture defined by 0.51λ/NA is 0.83μm with an NA of 0.3 and a wavelength of 488nm in the present system. The images of the focal spot at different focal planes are shown in Fig. 6(a). The experimental FWHM measurements of the focal spot with the focus shifts are shown in Fig. 6(b). The near diffraction limited focal spot (FWHM = 0.94 μm) at the original focal plane (Z = 0 μm) is achieved. Because the tilt angle of marginal rays increases with the focus shifts, the marginal rays lose their direction when the tilt angle exceeds the memory effect angle. This causes an increase of the focal spot size. The spot size is increased by 1.2 times at a depth of 0.5mm

Optics EXPRESS

with CAORF. However, a similar spot size is achieved only at the depth of 0.06mm for the conventional CAO system.

5.2 3D Multi-spot patterning

An advantage of using the SLM as a wavefront corrector is the ability to generate an arbitrary pattern through the scattering layer [17,29]. To generate a 3d pattern, the phase often needs to be measured at different Z planes because of the limited axial FOV. Sequential generation of the multi-spot pattern at different focal planes requires an update of the phase masks on the SLM, which limits the temporal resolution of the system. Here we show that CAORF can scan 3d patterns while scanning along the Z-axis with RF.

Figure 7(a) shows the configurations of the experiments. The whole aperture is divided into two groups of channels by random selection of the segments. The transmission matrix for each group is measured at two different focal planes separated by 120 μm. The combined phase masks generate two patterns at the two focal planes at 0 μm and 120 μm, respectively. The RF module scans two patterns simultaneously from 0 μm to 120 μm and 120 μm to 240 μm, respectively. The 3d patterns at different focal planes are confirmed by images from the camera as shown in Fig. 7(b). The detector objective lens translates along the optical axis to focus at each plane. The average intensity enhancement of the four focused spots at different depths is shown in Fig. 7(c). The intensity enhancement is calculated as the ratio of the intensity at the focus to the background intensity.

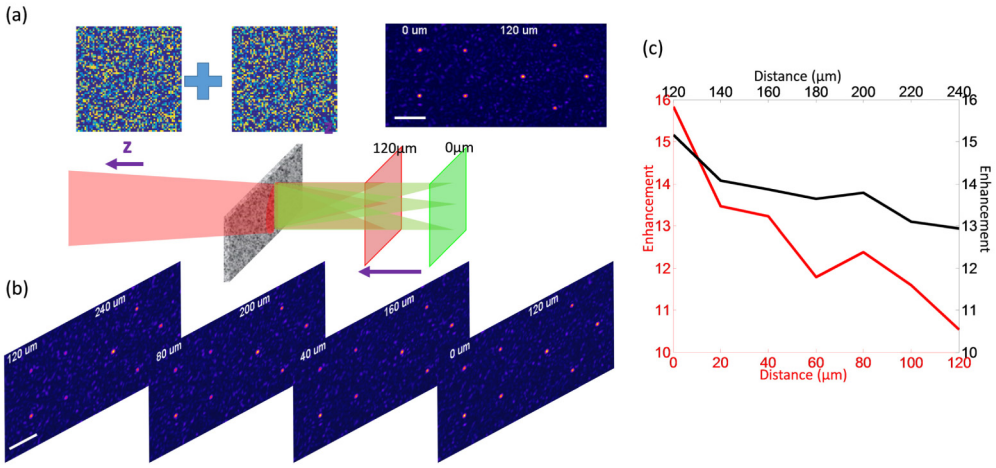

Fig. 7. Axial scanning of 3d patterns with RF. (a) Two patterns at two focal planes (Z = 0 μm and 120 μm) are generated simultaneously by combing two phase masks. The remote focusing module shifts the focal plane with a range of 120 μm. (b) The corresponding images at different focal planes are captured by the CCD camera. (c) The average intensity enhancement of the focal spots at different depth. The scale bar is 10 μm.

5.3 3DFluorescent Imaging through scattering tape

To evaluate the system performance for 3d fluorescent imaging through a scattering layer, a coverslip with 1.1 μm diameter fluorescent beads (FluoSpheres, Invitrogen) was placed at a 2mm distance behind the scattering tape. The emission light is collected by a detector after an emission filter as shown in Fig. 8(a). In the present system, the CCD camera works as the photodetector. To generate the final 2d image, the intensity at each scanning position is calculated as the sum of a large region of interest (100 × 100 pixels) centered at the focal spot on the CCD camera. In total 200 × 200 points are collected, which produced the final image with 200 × 200 pixels. The image before wavefront correction is shown in Fig. 8(b). It is hard to observe the fine structure because of scattering. Figure 8(c) shows the images when the scattering layer moves from 0 μm to 150 μm towards the sample. This is similar to axial

Optics EXPRESS

scanning by moving the sample. At a depth of 0 μm, the structure of the beads can be observed after correction when the SLM is conjugated with the scattering laser. The image contrast degrades quickly with an increase of the axial shift. At an axial shift of 150 μm, the fine structure cannot be observed as shown in Fig. 8(e). In the case of CAORF, the focal plane is moved toward the scattering layer by the RF module. The sample also moves the same distance using a translation stage. Figure 8(d) shows images at depths from 100 μm to 500 μm. As can be seen, the fine structure can be still observed even at a depth of 500 μm as shown in Fig. 8(f). The transmission microscope image of the same area in Fig. 8(g) shows the similar structure.

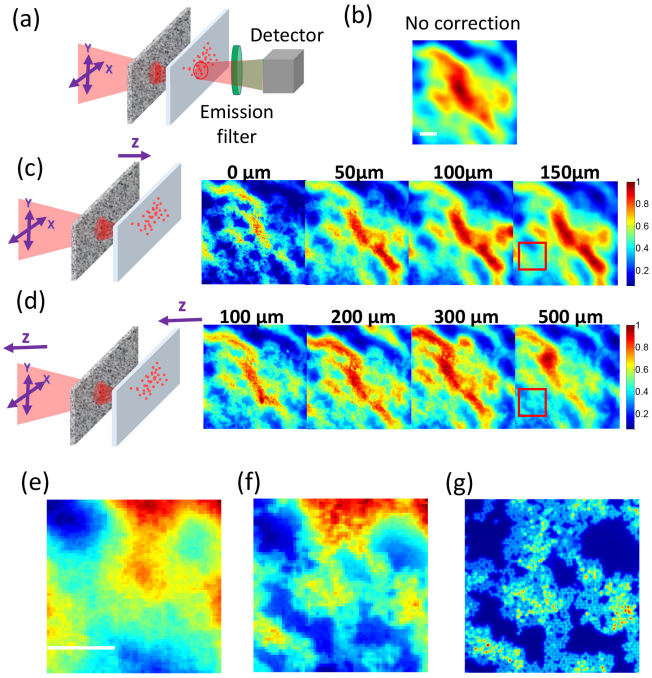

Fig. 8. Comparison of 3d fluorescent imaging with CAO and CAORF. (a) The sample is placed 2mm behind the scattering layer. The beam is translated in the *X*-*Y* plane by the 2d scanning module. The emission light is collected by the detector, which gives the intensity information for each scan position to generate a 2d image. (b) The image without wavefront shaping. (c) The images at depths of 0 μm, 50 μm, 100 μm and 150 μm without RF. The depth is adjusted by moving the scattering layer. (d) The images at depths of 100 μm, 200 μm, 300 μm and 500 μm with CAORF. The depth is adjusted by the remote focusing module. (e) and (f) Enlarged views of the areas highlighted in (c) and (d), respectively. (g) The transmission microscope image of the same area. The scale bar is 50μm.

5.4 Two-photon imaging through a mouse skull

To test the ability of imaging through biological tissue, additional modifications have been made on the original system (as shown in Fig. 13(b) in appendix C). Two galvanometers with relay lenses are integrated into the system to provide high-speed imaging ability. Using epifluorescence for phase shaping is more practical for biological imaging, and nonlinear optical feedback is more suitable for the epidetection geometry to achieve diffraction-limited focusing through scattering samples [20]. Therefore, a photomultiplier tube with additional lenses is installed near a 25x water-immersion objective (XLPLN25XWMP, NA 1.05, Olympus). A Ti:Saphhire laser (Chameleon Ultra II, Coherent) is used to generate a two-photon fluorescence signal for both phase optimization and imaging. An iterative phase optimization procedure is used to achieve an enhanced focus using the weak two-photon

Optics EXPRESS

signal [37,38]. A mouse skull with a thickness of 130μm is mounted on a 170μm thick coverslip with UV-activated glue (Fotoplast Gel, Dreve, part number 44691). The scattering mean free path of the mouse skull is around 55 μm [31]. Agarose gel with 1.1 μm diameter fluorescent beads (FluoSpheres, Invitrogen) are mounted between the two coverslips. The location of the SLM is adjusted to the conjugate plane of the mouse skull. The phase optimization procedure is applied on the top surface of the agarose gel at a depth of 0μm. The laser beam is located at the center of the FOV, where no specific structure is observed as shown in Fig. 9(c). After applying the final phase shown in Fig. 9(b), the microspheres can be clearly observed in Fig. 9(c). We then keep the initial phase on the SLM and shift the focal plane using the remote focusing lens (CAORF) and sample stage (CAO), respectively.

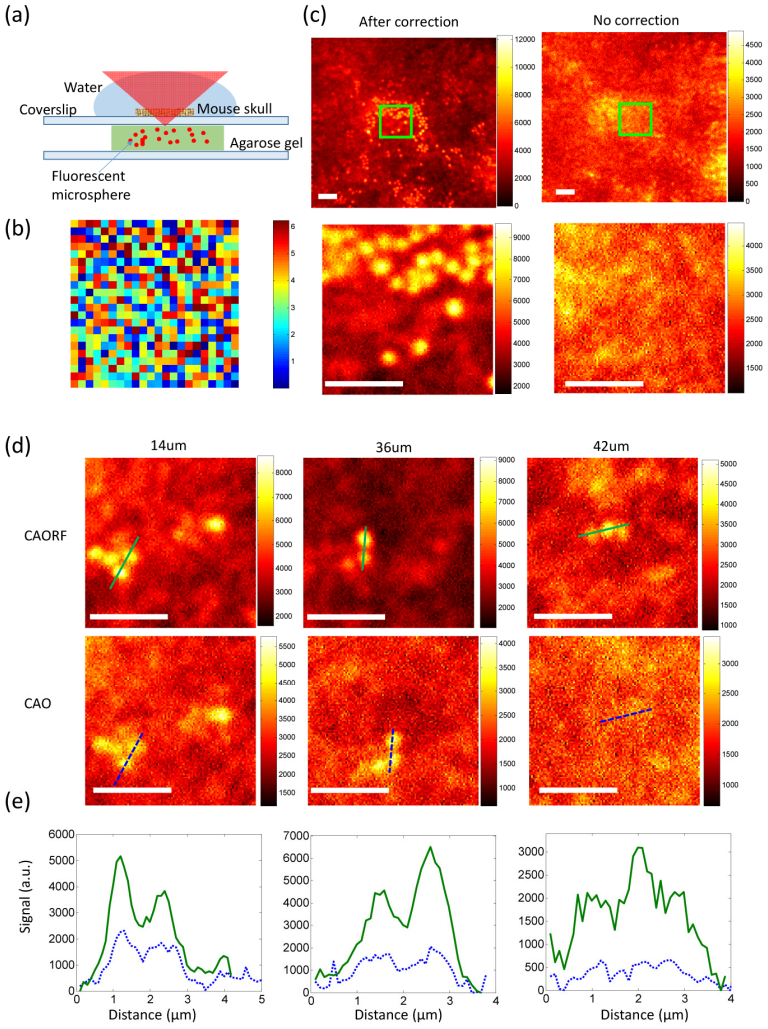

Fig. 9. Two-photon imaging of fluorescent microspheres through a mouse skull. (a) A schematic diagram of the imaging configuration. A piece of mouse skull is mounted on a 170 μm thick coverslip. Agarose gel with a thickness of 3mm is sandwiched between two coverslips. The initial correction is applied on the microspheres just below the first coverslip. (b) The phase for compensation of the scattering. (c) The images of microspheres at the top of the agarose gel (depth = 0 μm) with and without correction. The green boxes indicate the enlarged view. (d) Images at depths of 14 μm, 36 μm and 42 μm with the CAORF system and the conventional CAO system. (e) The intensity profile along the line indicated in (d). The scale bar is 5 μm.

Optics EXPRESS

Figure 9 (d) shows images at depths of 14 μm, 36 μm and 42 μm in both configurations. The image quality from CAORF is much better than conventional CAO. At a depth of 42 μm, the microspheres can still be observed by CAORF but cannot be observed by CAO. Figure 9(e) shows the intensity profile along the line in Fig. 9(d). The intensity improvements are 2.2, 3.2 and 4.7 at depths of 14 μm, 36 μm and 42 μm, respectively.

6. Discussion and conclusions

By the combination of conjugate AO and RF, the CAORF system maintains the conjugation between the scattering layer and the SLM during axial scanning, which can provide an extended axial FOV. No additional update of the phase on the SLM is required. The axial scanning speed is only limited by the remote focusing module. As a proof-of-concept system, a single lens on a three-axis translation stage was used for the RF and 2d scanning. It can easily be replaced by a high-speed RF module, such as an acousto-optic deflector (AOM) [39,40], an electrically tunable lens [41,42], an ultrasound lens [43] or a reference lens with an axial scan mirror [44]. The lateral scanning speed can be improved by using a high-speed resonant scanner or an AOM [45]. In this paper, we also demonstrate three-dimensional multi-spot formation through a scattering layer. The results show its potential application in multiplane structural imaging with the ability for scattering and refractive aberration compensation [46].

In the memory effect, the FOV depends on both the thickness of the scattering layer and the distance between the scattering layer and the structure that is imaged. For highly scattering layers, it is important to keep the structures that are imaged far from the scattering layer. Fortunately, the effective thickness of biological tissues are often much smaller than their physical thickness [31]. Ballistic light can still penetrate through the tissue. It has been reported that the effective thickness of a mouse skull is only 2.3μm [31]. This allows a wider FOV even when the target to be imaged is close to the scattering layer. Although we show the compensation of scattering, the present system can also correct low-order refractive aberration as well. Compared with existing CAO microscopy systems [47–49], the proposed system can achieve a larger axial FOV by minimizing the conjugation error during axial scanning.

In addition to the memory effect, the axial FOV is also limited by system aberration from the objective lens, which is not discussed in this paper. Theoretically, the wavefront for the system aberrations could be calibrated and added onto the SLM during wavefront shaping for scattering compensation. For a thick sample with multiple scattering, a numerical study has shown that multi-conjugate AO, originally used in astronomy, could be a promising solution [50]. The proposed configuration in this paper could also benefit these systems to achieve a large FOV with near diffraction-limited resolution.

In conclusion, we have demonstrated a large volume wavefront shaping method by combining CAO and RF. This configuration minimizes the conjugation error during axial scanning and provides a much larger axial FOV. Compared with a system without RF, the experiments show a 10x axial FOV improvement for 16,384 input channels on the SLM when a single layer of Scotch tape is used as a scattering layer. We demonstrated three-dimensional multi-spot patterning through the scattering layer. The result of three-dimensional fluorescent imaging shows its ability to extend the axial FOV for laser scanning microscopy. We have also demonstrated two-photon imaging through mouse skull tissue and showed that CAORF improves the image quality and has the ability to image deeply through biological scattering tissue.

Optics EXPRESS

Appendix

A. Intensity degradation caused by the axial shift for CAO without RF

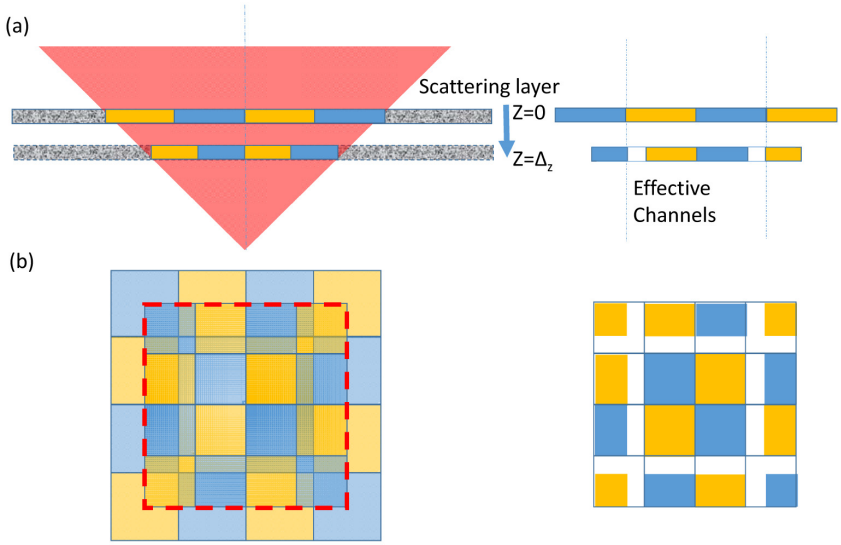

Fig. 10. Effective segments change due to the conjugation error from an axial shift. (a) & (b) show the effective segments in one and two dimensional space, respectively.

The electric field at the output channel, E_{out}, can be considered to be the sum of the contributions from all the input channels, which is given by [51]:

$$E_{out} = TE_{in} = \sum\nolimits_n t_n E_{in}^n, \tag{6}$$

where T and E_{in} are the transmission matrix and input electric field, respectively. The complex phasor t_n follows a circular Gaussian distribution [17].

To focus light through the scattering layer, a conjugate electric field is generated on each channel, $E_{in}^n = Ae^{-i\arg(t_n)}$. The output field after optimization can be written as:

$$E_{ideal} = A\sum\nolimits_n |t_n|. \tag{7}$$

When the conjugate plane shifts during axial scanning, the effective segments becomes smaller, which decreases the amplitude of the input channel as shown in Fig. 10. Then the output field can be rewritten as:

$$E_{\Delta z} = A\sum\nolimits_n \alpha_{n,\Delta z} |t_n|, \tag{8}$$

where $\alpha_{n,\Delta z}$ is the ratio of the effective area to the segment area at the n^{th} segment, which can be calculated numerically. The intensity degradation for the axial shift Z can be calculated as:

$$\eta_{\Delta z} = \frac{\left\langle E_{\Delta z}{}^2 \right\rangle}{\left\langle E_{ideal}{}^2 \right\rangle} \sim \left(\frac{\sum_n \alpha_{n,\Delta z}}{N} \right)^2. \tag{9}$$

Optics EXPRESS

B. Theoretical calculation of axial FOV for CAORF

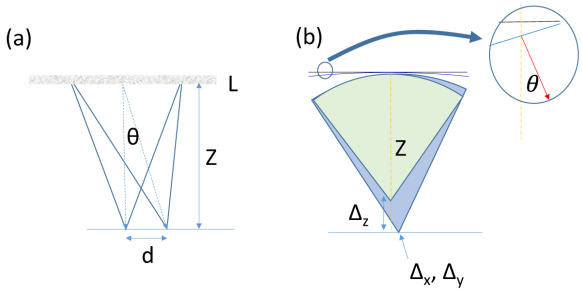

Fig. 11. Calculation of the correlation function based on the memory effect. (a) The original configuration using an angular FOV. (b) The general configuration for three-dimensional scanning.

The angular FOV can be calculated using the memory effect as follows [23,24]:

$$C_\theta(\theta, L) = k\theta L \Big/ \sin h(k\theta L), \tag{10}$$

where L is the effective thickness and θ is the field angle as shown in Fig. 11(a). During three-dimensional scanning as shown in Fig. 11(b), defocus and tip/tilt phases are added to the conjugate plane by the RF module and 2d scanner, which are defined by [27]:

$$\phi = \frac{k\rho^2\Delta_z}{2Z(Z-\Delta_z)} + \frac{k(x\Delta_x + y\Delta_y)}{Z} \tag{11}$$

where x and y are the coordinates on the conjugate plane. Z is the distance between the scattering layer and the focal spot at the initial focal plane. Δ_x, Δ_y and Δ_z are lateral and axial shifts. $\rho = \sqrt{x^2 + y^2}$. Now we can separate the whole conjugate plane into multiple small segments and numerically calculate the correlation function as:

$$C_{x,y,z}(\Delta_x, \Delta_y, \Delta_z) = \frac{\iint C_\theta(d\phi \big/ d\rho, L)dxdy}{\iint C_\theta(0, L)dxdy} \tag{12}$$

The change of the effective segments because of lateral and axial shifting can be also considered when calculating the correlation function using the equation above. The effective thickness of the scattering layer can be measured by fitting the correlation function at the initial focal plane. Figure 12(a) shows the measurement and the fitted correlation function. The effective length of the scattering layer, L, is around 5 μm. The normalized intensity along X and Z axis shift calculated by (12) is shown in Fig. 12(b).

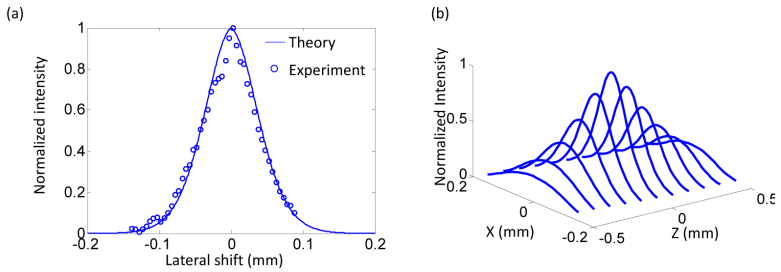

Fig. 12. (a) Normalized intensity versus lateral shift and (b) Normalized intensity along the X and Z plane.

Optics EXPRESS

C. System setup diagram

Figure 13 shows the system setup diagram below.

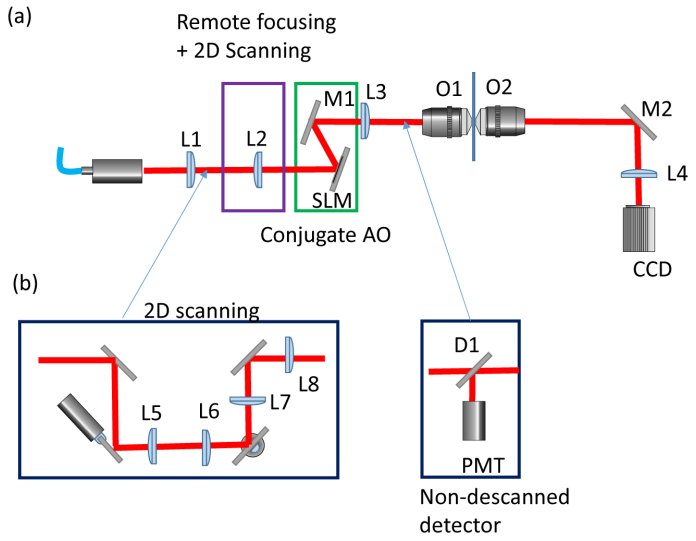

Fig. 13. System setup diagram. (a) The setup used for system evaluation. A lens (L1) collimates the laser beam from a 488nm solid-state laser. A lens (L2) installed on a three-axis translation stage works as a remote focusing (RF) and two-dimensional (2D) scanning module. The conjugate AO module consists of a spatial light modulator (SLM) and a folding mirror (M1), which are installed on a single-axis translation stage. The lens (L3) and an objective lens (O1) image the SLM plane onto the scattering layer. The light is collected by another objective lens (O2) and focused by a lens (L4) onto a CCD camera. (b) The additional modification for two-photon imaging through a mouse skull sample. Two galvanometers are used for fast scanning. L5 and L6 are relay lenses between the two scanners. Lens L7 and L8 direct the beam to the remote focusing lens (L2). A photomultiplier (PMT) and a dichroic mirror (D1) are added to the system to collect the emission light from the sample.

Funding

W. M. Keck Foundation; National Science Foundation Grant Numbers 1353461 and 1429810.

Acknowledgments

The results presented herein were obtained at the W. M. Keck Center for Adaptive Optical Microscopy (CfAOM) at University of California Santa Cruz. The CfAOM was made possible by the generous financial support of the W. M. Keck Foundation. We would like to thank Prof. Yi Zuo and Dr. Ju Lu of MCD Biology at UCSC for the mouse skull tissue samples that were used in these experiments. Any opinions, findings, and conclusions or recommendations expressed in this material are those of the authors and do not necessarily reflect the views of the National Science Foundation.